PHOTONICS Research

Embedded whispering-gallery mode microsphere resonator in a tapered hollow annular core fiber

Jiawei Wang,[1] Xiaobei Zhang,[1,*] Ming Yan,[1] Lei Yang,[1] Fengyu Hou,[1] Wen Sun,[1] Xiaotong Zhang,[2] Libo Yuan,[3] Hai Xiao,[4] and Tingyun Wang[1]

[1]Key Laboratory of Specialty Fiber Optics and Optical Access Networks, Joint International Research Laboratory of Specialty Fiber Optics and Advanced Communication, Shanghai Institute for Advanced Communication and Data Science, Shanghai University, Shanghai 200444, China
[2]The Key Laboratory of In-Fiber Integrated Optics, Ministry of Education, College of Science, Harbin Engineering University, Harbin 150001, China
[3]School of Electronic Engineering and Automation, Guilin University of Electronic Technology, Guilin 541000, China
[4]Department of Electrical and Computer Engineering, Clemson University, Clemson, South Carolina 29634, USA
*Corresponding author: xbzhang@shu.edu.cn

Received 31 August 2018; revised 12 October 2018; accepted 13 October 2018; posted 16 October 2018 (Doc. ID 344719); published 19 November 2018

We propose and demonstrate a tapered hollow annular core fiber (HACF) coupler for excitation of whispering-gallery modes (WGMs) of an embedded microsphere resonator. The coupler is simply fabricated by fusion splicing of a segment of HACF with the single-mode fiber (SMF), and then improved by tapering the splicing joint to reduce the cone-apex angle. Therefore, the coupling efficiency from the SMF to the HACF is enhanced to excite various WGMs via evanescent field coupling. Normal positive, negative symmetrical Lorentzian and asymmetric Fano line shapes can be obtained by varying the resonator size and location. Another interesting phenomenon is observed that a higher *Q*-factor mode in a lower *Q*-factor mode has a contrast as high as 58. Temperature sensing with good stability is also demonstrated. This embedded WGM microsphere resonator in the tapered HACF is expected to promote environmental adaptability in practical applications due to its simplicity and robustness.

https://doi.org/10.1364/PRJ.6.001124

1. INTRODUCTION

Optical whispering-gallery mode (WGM) resonators confine the electromagnetic wave by continuous total internal reflection at the resonator edge [1,2], and usually have symmetrical Lorentzian [3,4], asymmetric Fano [5–8], and electromagnetically induced transparency (EIT) line shapes [9–11]. Due to extremely high values of the *Q*-factor and small mode volumes of WGMs, they also have broad application prospects for filters [12], sensors [4,13–15], low-threshold lasers [16–18], cavity optomechanics [19,20], and nonlinearities [21,22]. It is particularly important to couple the light from the outside into resonators to excite WGMs. Common WGM excitation schemes are generally based on phase-matching of the evanescent fields, for example, using prisms [23], fiber tapers [11], D-shaped fiber [6,24], angle polished fiber [25], optical waveguides [10], free-space coupling [26], and chaos-assisted broadband momentum transformation [27]. The above coupling method is, however, less robust, and the resonance wavelength can shift or even disappear due to external air flow, dust, or slight movements and vibrations of the coupler. So some methods have been proposed to improve the robustness, such as using glue encapsulation [28].

Recently, some novel coupling methods have been proposed, such as attaching microspheres on the end of micro-structured optical fibers, of which the coupler is robust and gets a *Q*-factor of 500 [29]. Furthermore, the microsphere is embedded into micro-structured optical fibers, and the *Q*-factor increases to 2.2×10^3 [30]. In order to enhance the robustness and *Q*-factor, the microsphere is encapsulated inside a photonic crystal fiber (PCF) [31] or a silica capillary [32–34] with a small inner diameter, both of which are fabricated by chemical etching, with a *Q*-factor of about 1.58×10^4 and 2.57×10^4, respectively. However, the chemical etching causes the coupling position and the reflective surface to be coarse. The core in the PCF and the fiber pigtailed thin wall are fragile. Moreover, the etching process is complicated. The key point is to couple the light into the resonator, while the hollow annular core fiber (HACF) [35] fortunately has an inner high-index core to confine the light with an opening to embed a resonator for exciting WGMs.

In this paper, an embedded WGM microsphere resonator in a tapered HACF is proposed for excitation of WGMs to avoid the etching process in the previous configurations and maintain a high robustness. First, we theoretically and experimentally study the effect of the taper length on the coupling efficiency

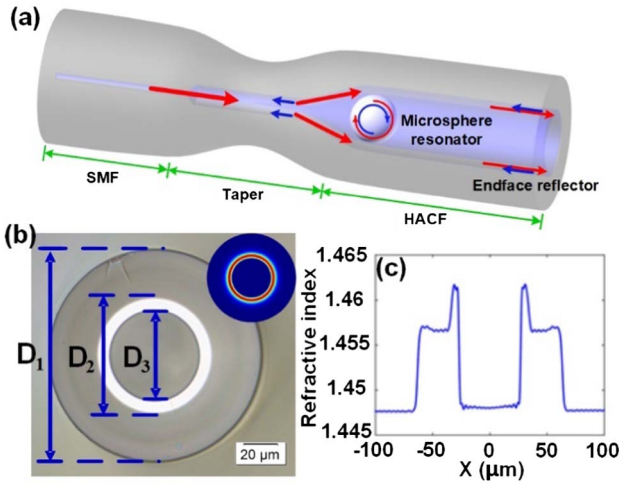

Fig. 1. (a) Schematic of the tapered HACF coupled microsphere resonator. (b) Cross-sectional view with the inset as the simulated mode field distribution and (c) RI profile of HACF.

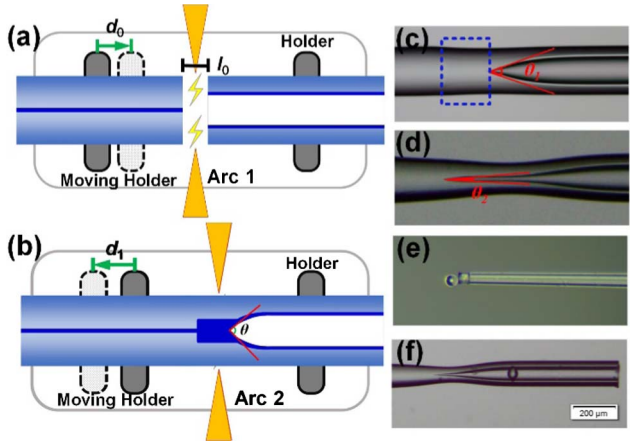

Fig. 2. (a) Schematic of splicing HACF with SMF. (b) Schematic of tapering the area, with the cone-apex angle as θ and the single tapering distance as d_1. (c) Micrograph of SMF-HACF transition area without tapering, with the multi-mode transition area highlighted in the blue dotted box. Micrographs of (d) SMF-HACF transition area with tapering, (e) microsphere resonator manipulated by a section of tapered fiber, and (f) microsphere resonator embedded into the coupler.

between the single-mode fiber (SMF) and HACF. Second, the effects of the size and embedded position of the microsphere resonator on the reflection spectra are also investigated in both theory and experiment. As the high-index annular core restricts light energy to several micrometers to excite the evanescent wave, it is possible to realize the robustness of the device and the easiness of the effective coupling between the microsphere and the HACF.

Figure 1(a) shows the schematic structure of the microsphere resonator embedded in the tapered HACF. The device is composed of a section of SMF (Corning, SMF-28), a section of HACF, and a barium titanate glass microsphere with a refractive index (RI) n_{eff} of 1.93. The scattering loss is the dominant reason for the final Q-factor, as the intrinsic radiative loss and absorption loss are much smaller. The HACF has a low RI SiO_2 cladding with its diameter D_1 of 125 μm, a high RI doped SiO_2 annular core with its diameter D_2 of 66 μm, and an air hole with its diameter D_3 of 54 μm as shown in Fig. 1(b). The simulated cross-section mode (fundamental mode) profile of the HACF can be seen in the inset. The RIs of the HACF annular core n_{core} and cladding n_{clad} are measured as 1.462 and 1.457 as shown in Fig. 1(c). It is worth noting that the RI of the air core is denoted as 1.448 because the RI profile is measured with the matching liquid. The input beam enters into the HACF annular core from the SMF, through the taper region, and couples into the microsphere through the evanescent wave via the inner annular core, and the other light is reflected at the HACF end face and couples into the microsphere again. Expected WGMs can be excited as a result of the anterior resonance principle.

2. FABRICATION AND SIMULATION OF THE COUPLER

The fabrication process of the device is illustrated in Fig. 2. First, a segment of HACF is fusion spliced with a segment of SMF by a commercial fusion splicer (FITEL-S178) as shown in Fig. 2(a), with the distance l_0 between end faces as about 10 μm and the propulsion distance of fiber d_0 as 15 μm. The splicing parameters include an arc power of 100, a prefuse time of 100 ms, and an arc time of 500 ms. Arc 1 is slightly modified from the SMF splice mode to perform a splice with a sharp cone-apex angle θ in the transition area as shown in Fig. 2(b). The cone shape arises from the incomplete collapse of the annular core of HACF near the electrodes. However, the cone-apex angle θ_1 is measured to be up to 34°, though the welding parameters are optimized, which results in a low coupling between the SMF and the HACF. Moreover, the light will directly transmit into the air hole due to the large angle. It is found that Fabry–Perot-type reflection can be observed when the microsphere resonator is embedded into this structure. An intuitive method to solve this problem is to taper the coupling region between the SMF and HACF. During the tapering experiment, the arc 2 intensity is weak, so the arc power is adopted as 5, the prefuse time as 50 ms, and the arc time as 200 ms to prevent excessive collapse, and the single tapering distance d_1 is adopted as 100 μm. Due to the elasticity of silica material, the actual tapered length is in fact less than 100 μm. The HACF is then cut to a desirable length as about 500 μm, and fixed on a precision fiber alignment stage (M-562, Newport). We operate a fiber taper on another stage to attach the microsphere with the diameter from 45 to 54 μm through van der Waals force, and embed it into the air hole of HACF, under a CCD as shown in Fig. 2(e). The fabricated device can be seen in Fig. 2(f).

To verify the enhancement of the coupling efficiency, we simulate the coupling efficiency as a function of the cone-apex angle θ, using the commercial software (Rsoft, BeamProp module) as shown in Fig. 3. Simulation parameters including the RI and sizes are the same as in Fig. 1. The energy distribution at 1550 nm can be seen in the inset of Fig. 3(a). An interesting phenomenon is that the total reflection condition at the interface between cladding and annular core is destroyed when the

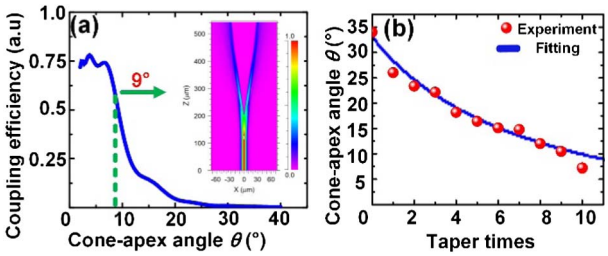

Fig. 3. (a) Simulation of the coupling efficiency as a function of cone-apex angle θ, with the inset as the energy distribution in the device. (b) Taper times versus the cone-apex angle θ by experimental and theoretical fitting results.

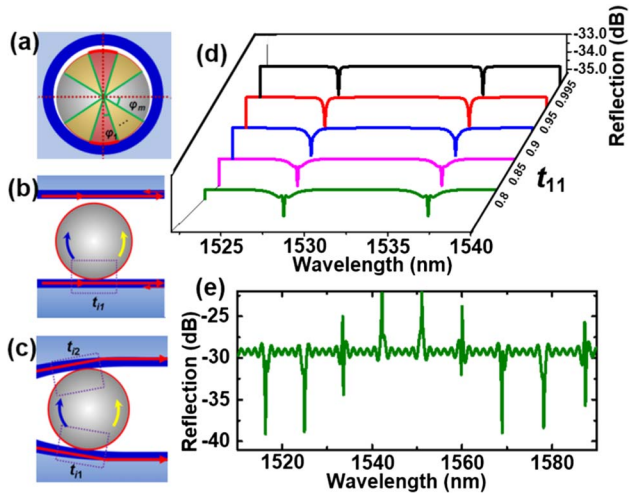

Fig. 4. (a) Cross section of the model. (b),(c) Model of the microsphere (b) without and (c) with being locked by the HACF. (d) Evolution of reflection spectra with t_{11} from 0.8 to 0.995 for the case of (b). (e) Reflection spectrum for the case of (c).

angle exceeds 9°, which can be estimated by the formula of the total reflection condition $\theta_c = 2\arccos(n_{\text{clad}}/n_{\text{core}})$. Therefore, two fusion splicing arcs are necessary for decreasing the cone-apex angle to meet the condition of high-efficiency coupling of incident light. As the angle is large, a portion of the light energy is transmitted to the air core at the fusion point and forms a Fabry–Perot cavity with three mirrors after embedding the microsphere into the HACF. When the angle is small and less than about 9°, there are several peaks because the periodic reflection of light in the annual core constitutes a damping oscillation function related to the propagation length, as shown in Fig. 3(a).

In addition, the collapse deforms into a high RI cylindrical core with a diameter of about 42.1 μm; it can be seen in the blue dotted box in Fig. 2(c). It is calculated and excellently validated by the volume conservation formula $[\pi D_4^2/\pi D_1^2 = (\pi D_2^2 - \pi D_3^2)/(\pi D_1^2 - \pi D_3^2)]$, with D_4 as the cylindrical core diameter. As the diameter of the collapsing core is much larger than that of an SMF core, the two modes will not match well, which makes the coupling of reflection light difficult [36]. Figure 3(b) shows the relationship between the tapering length and the cone-apex angle based on the experiment and fitting with $\theta = 2\arctan[a/(b+L)]$, where b and a are the width and half height of the cone area without tapering, and L is the tapering length. We find that after several times of tapering operation, the cone-apex angle decreases gradually to 7°, and if we try another tapering, it will completely collapse. In Fig. 2(d), the device is shown after more than 10 times tapering and obtains a high-efficiency coupling with the θ_2 at about 7°, which satisfies the high coupling condition as shown in Fig. 3(a). Meanwhile, it will also increases the efficiency of reflection light coupling by decreasing the diameter of the collapsing core from 42.1 μm to around 20.0 μm.

3. THEORETICAL MODEL AND ANALYSIS

The normalized reflection with the transfer matrix method (TMM) is used to analyze the proposed device, similar to the previous work [37]. When there is no microsphere resonator in the coupler, the reflection spectrum is a relatively flat straight line caused by the end face. However, a WGM-associated phenomenon will appear after embedding the microsphere resonator. As shown in Fig. 4(a), the cross section of the coupling between the resonator and HACF generally has different coupling gaps in a whole circumference for the case of a resonator size smaller than the air hole. To solve this problem, we divide the cross section as m parts in a quadrant, with the corresponding angle of the coupling region between the microsphere and the HACF as φ_i $(i = 1, \ldots, m)$. The normalized reflection P_R can be obtained as follows:

$$P_R = \left| \sum_{i=1}^{m} \frac{2\varphi_i}{\pi} \left\{ \frac{re^{2j\delta}}{2} \left[\left(\frac{t_{i1} - \tau t_{i2} p^2}{1 - \tau t_{i1} t_{i2} p^2} \right)^2 + \left(\frac{t_{i2} - \tau t_{i1} p^2}{1 - \tau t_{i1} t_{i2} p^2} \right)^2 \right] - \frac{\sqrt{\tau(1 - t_{i1}^2)(1 - t_{i2}^2)}\, p}{1 - \tau t_{i1} t_{i2} p^2} \right\} \right|^2, \quad (1)$$

where r is the amplitude reflectivity at the HACF end face satisfying $r = (n_{\text{core}} - n_{\text{air}})/(n_{\text{core}} + n_{\text{air}})$, with n_{air} as the RI of air. t_{i1} and t_{i2} are the equivalent amplitude transmission coefficients for part i, under the condition of lossless coupling. When the gap between the microsphere and the inner wall is too large to be coupled, the equivalent amplitude transmission coefficient is equal to 1. τ is the resonator round-trip transmission coefficient. p is the halfway phase factor satisfying $p = \exp(i2\pi^2 n_{\text{eff}} R/\lambda)$. R and λ are the radius of the microsphere and the wavelength in vacuum, respectively. δ and L_1 are the phase difference and distance from the resonator–HACF coupling point to the end face of the HACF, respectively, with $\delta = 2\pi n_{\text{core}} L_1/\lambda$.

Two typical cases are considered as shown in Figs. 4(b) and 4(c). The microsphere is not locked by HACF when the diameter of the microsphere is smaller than the inner diameter D_3 as shown in Fig. 4(b). Since the upper part of the microsphere is far enough from the HACF inner wall that it cannot be coupled, t_{i2} is equal to 1. In the simulation, the quadrant is divided into three parts, with φ_1, φ_2, and φ_3 adopted as 1°, 10°, and 79°, respectively. We investigate the theoretical characteristics as a function of t_{11} from 0.8 to t_{21}, with t_{21} and t_{31} adopted as 0.995 and 1, respectively. Other parameters used in

the simulation are chosen as $L_1 = 100$ μm, $R = 22.40$ μm, and $\tau = 0.995$. Evolutions of reflection spectra are obtained as shown in Fig. 4(d), which reveals a higher Q mode in a relatively lower Q mode, arising from the two different coupling parts with different coupling coefficients. Due to the relation between t and the corresponding Q-factor satisfying $Q \sim \sqrt{\tau t}/(1-\tau t)$, the higher the coupling efficiency, the higher the Q value. Another case corresponds to the situation of the microsphere fully locked by HACF, for example, in the cone region of the coupler as shown in Fig. 4(c). Therefore, the microsphere is in close contact with the inner wall. We assume $\varphi_1 = 90°$, $\varphi_2 = \varphi_3 = 0°$, $t_{11} = 0.995$, $\tau = 0.95$, $L_1 = 456$ μm, and $R = 21.15$ μm. Various types of resonance shapes can be obtained as shown in Fig. 4(e), including symmetrical Lorentzian and asymmetric Fano line shapes. Besides, positive and negative Lorentzian line shapes are also found with peaks and dips corresponding to resonance wavelengths [8].

4. EXPERIMENTAL RESULTS

In the experiment, we embed the microsphere into the tapered HACF and observe the reflection spectra through the optical sensing analyzer (si125, Micron Optics, Inc.) in real time. Figure 5(a) shows the experimental and simulated reflection spectra with the microsphere with a diameter of ~42.3 μm, which is slightly smaller than the HACF inner diameter D_3. A Lorentzian line shape with a free spectral range (FSR) of 9.00 nm and Q-factor of about 13,000 is obtained. There are also resonance peaks due to high-order modes. By the formula of FSR and the diameter of the microsphere [FSR $= \lambda^2/(2\pi n_{\text{eff}} R)$], it is found that the size of the microsphere matches the experimental results well.

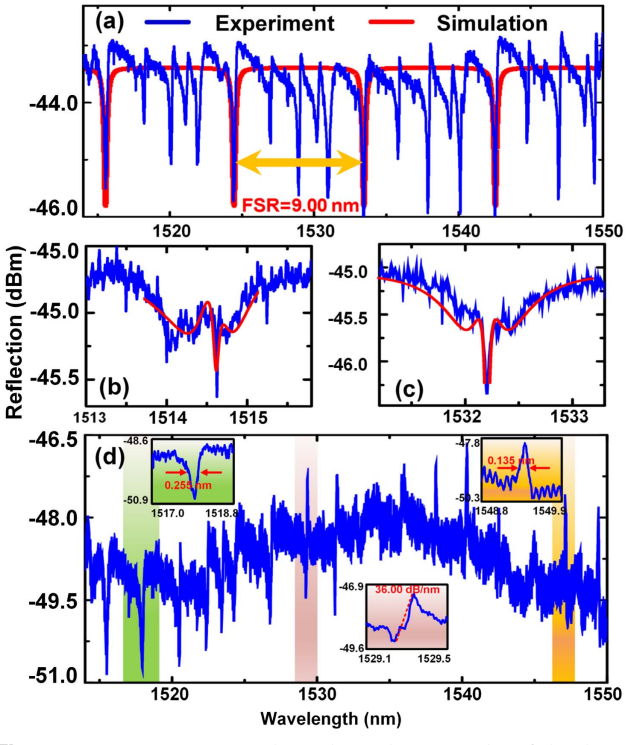

Fig. 5. (a) Experiment results and simulation results of the device with a 42.30 μm diameter microsphere in the position very close to the end face. Experiment results of the device with a 42.60 μm diameter microsphere in the position very close to the end face, shown as symmetric Lorentzian line shapes with Q-factors about (b) 1300 and 76,000, and (c) 1700 and 35,000. (d) Experiment results of the device with microsphere locked by HACF inner wall with insets corresponding to detailed views of the negative symmetrical Lorentzian, asymmetrical Fano, and positive symmetrical Lorentzian line shapes.

Furthermore, another larger microsphere with a diameter of ~42.6 μm is inserted with the reflection spectra shown in Figs. 5(b) and 5(c). As the microsphere is bigger, the coupling region increases, and hence the equivalent amplitude transmission coefficient t decreases. As shown in Fig. 5(b), the reflection spectrum is formed by a higher Q-factor mode in a lower Q-factor mode with a contrast as high as 58. The center of both resonance wavelengths has a deviation of 0.25 nm, due to the irregularity of the microsphere shape or distance from the resonator–HACF coupling point to the end face of the HACF. Two modes with different radial numbers and hence different Q-factors can also be possible reasons. Because the Q-factor between the two resonances is quite different, two small peaks are generated on the two sides of the high Q-factor resonance peak. The reflection spectrum is also formed by a higher Q-factor mode in a lower Q-factor mode with nearly the same resonance wavelength, as shown in Fig. 5(c). And the intensity of the higher Q-factor mode is quite large, which is different from the interference peak as EIT [10]. These results have been well theoretically predicted as shown in Fig. 4(d). If the microsphere continues to be embedded into the depth by the fiber taper until being locked by the HACF inner wall, a symmetrical Lorentzian line shape and asymmetric Fano line shape can be observed as shown in Fig. 5(d). This is in good agreement with the simulation as shown in Fig. 4(e). Insets show the detailed negative and positive symmetrical Lorentzian line shapes around 1517.90 nm and 1549.85 nm, with full width at half-maximum of 0.255 nm and 0.135 nm, respectively, while the asymmetric Fano line shape around 1529.30 nm has a slope about 36.0 dB/nm.

The fabricated device is then placed into the temperature cabinet (ESL-04KA) for characterizing its temperature sensing properties. As the temperature increases from −50°C to 80°C with a step of 10°C, the resonant dip around 1532.5 nm shows a red shift with a sensitivity of 10.8 pm/°C, as shown in Fig. 6. The temperature sensitivities of each resonant dip or peak are nearly the same. The reason for the red shift of the resonance wavelengths is the change of the optical path caused by the

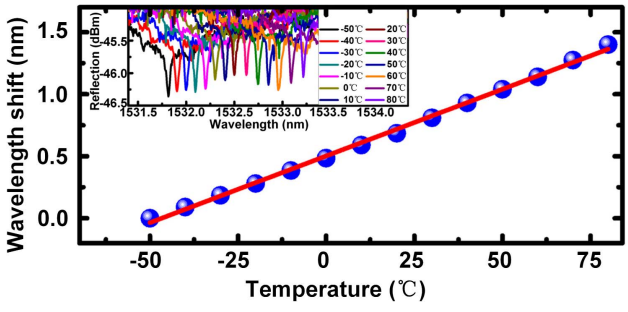

Fig. 6. Temperature response of the device, with inset as the reflection spectra under different temperatures.

thermo-optical effect and the thermal-expansion effect of the microsphere. Even if the device experiences several temperature changes and vibrations in the experiment, it still has good stability and robustness, due to the unique HACF coupling structure.

5. CONCLUSION

In summary, we demonstrate an embedded WGM microsphere resonator in a tapered HACF, through the circularly peripheral contact between the microsphere and the supporting annular core. By tapering the splicing joint to sharpen the cone-apex angle for increasing the coupling, periodical symmetrical Lorentzian and asymmetric Fano line shape resonances are observed and well validated by a transfer matrix model. A higher Q-factor mode in a lower Q-factor mode that has contrast as high as 58 is also obtained. Temperature sensing with good stability and robustness is also demonstrated. Besides the advantage of the reflection mode [38], the merits of this fiber-based device also include good integration and being alignment-free and etching-free, making it simple in processing and robust in structure, which shows broad potential for WGM-related applications such as sensors, optical filters, and lasers.

Funding. National Natural Science Foundation of China (NSFC) (61675126, 61735009, 61875116); Natural Science Foundation of Shanghai (18ZR1415200).

REFERENCES

1. A. B. Matsko and V. S. Ilchenko, "Optical resonators with whispering-gallery modes-part I: basics," IEEE J. Sel. Top. Quantum Electron. **12**, 3–14 (2006).
2. K. J. Vahala, "Optical microcavities," Nature **424**, 839–846 (2003).
3. S. Levy, M. Klebanov, and A. Zadok, "High-Q ring resonators directly written in As_2S_3 chalcogenide glass films," Photon. Res. **3**, 63–67 (2015).
4. Q. Lu, M. Li, J. Liao, S. Liu, X. Wu, L. Liu, and L. Xu, "Strong coupling of hybrid and plasmonic resonances in liquid core plasmonic microbubble cavities," Opt. Lett. **40**, 5842–5845 (2015).
5. J. Liao, X. Wu, L. Liu, and L. Xu, "Fano resonance and improved sensing performance in a spectral-simplified optofluidic micro-bubble resonator by introducing selective modal losses," Opt. Express **24**, 8574–8580 (2016).
6. L. Shi, T. Zhu, D. Huang, C. Liang, M. Liu, and S. Liang, "In-fiber Mach-Zehnder interferometer and sphere whispering gallery mode resonator coupling structure," Opt. Lett. **42**, 167–170 (2017).
7. Y. L. Shang, M. Y. Ye, and X. M. Lin, "Experimental observation of Fano-like resonance in a whispering-gallery-mode microresonator in aqueous environment," Photon. Res. **5**, 119–123 (2017).
8. K. Zhang, Y. Wang, and Y. H. Wu, "Enhanced Fano resonance in a non-adiabatic tapered fiber coupled with a microresonator," Opt. Lett. **42**, 2956–2959 (2017).
9. B. Peng, S. K. Özdemir, W. Chen, F. Nori, and L. Yang, "What is and what is not electromagnetically induced transparency in whispering-gallery microcavities," Nat. Commun. **5**, 5082 (2014).
10. S. Zheng, Z. Ruan, S. Gao, Y. Long, S. Li, M. He, N. Zhou, J. Du, L. Shen, and X. Cai, "Compact tunable electromagnetically induced transparency and Fano resonance on silicon platform," Opt. Express **25**, 25655–25662 (2017).
11. J. C. Knight, G. Cheung, F. Jacques, and T. A. Birks, "Phase-matched excitation of whispering-gallery-mode resonances by a fiber taper," Opt. Lett. **22**, 1129–1131 (1997).
12. S. Zhu, Y. Liu, L. Shi, X. Xu, S. Yuan, N. Liu, and X. Zhang, "Tunable polarization beam splitter based on optofluidic ring resonator," Opt. Express **24**, 17511–17521 (2016).
13. F. Vollmer and L. Yang, "Label-free detection with high-Q microcavities: a review of biosensing mechanisms for integrated devices," Nanophotonics **1**, 267–291 (2012).
14. S. Wan, R. Niu, H.-L. Ren, C.-L. Zou, G.-C. Guo, and C.-H. Dong, "Experimental demonstration of dissipative sensing in a self-interference microring resonator," Photon. Res. **6**, 681–685 (2018).
15. L. Shao, X. F. Jiang, X. C. Yu, B. B. Li, W. R. Clements, F. Vollmer, W. Wang, Y. F. Xiao, and Q. Gong, "Detection of single nanoparticles and lentiviruses using microcavity resonance broadening," Adv. Mater. **25**, 5616–5620 (2013).
16. F. Gu, F. Xie, X. Lin, S. Linghu, W. Fang, H. Zeng, L. Tong, and S. Zhuang, "Single whispering-gallery mode lasing in polymer bottle microresonators via spatial pump engineering," Light Sci. Appl. **6**, e17061 (2017).
17. F. Xie, F. Gu, H. Wang, N. Yao, S. Zhuang, and W. Fang, "Single-mode lasing via loss engineering in fiber-taper-coupled polymer bottle microresonators," Photon. Res. **5**, B29–B33 (2017).
18. X. F. Jiang, Y. F. Xiao, C. L. Zou, L. He, C. H. Dong, B. B. Li, L. Yan, F. W. Sun, Y. Lan, and Q. Gong, "Highly unidirectional emission and ultralow-threshold lasing from on-chip ultrahigh-Q microcavities," Adv. Mater. **24**, OP260–OP264 (2012).
19. H. Rokhsari, T. J. Kippenberg, T. Carmon, and K. J. Vahala, "Theoretical and experimental study of radiation pressure-induced mechanical oscillations (parametric instability) in optical microcavities," IEEE J. Sel. Top. Quantum Electron. **12**, 96–107 (2006).
20. A. Schliesser and T. J. Kippenberg, "Cavity optomechanics with whispering-gallery-mode optical micro-resonators," in *Atomic, Molecular, and Optical Physics* (2010), Vol. **58**, pp. 207–323.
21. R. Wolf, I. Breunig, H. Zappe, and K. Buse, "Cascaded second-order optical nonlinearities in on-chip micro rings," Opt. Express **25**, 29927–29933 (2017).
22. X. Xue, X. Zheng, and A. M. Weiner, "Soliton trapping and comb self-referencing in a single microresonator with $\chi^{(2)}$ and $\chi^{(3)}$ nonlinearities," Opt. Lett. **42**, 4147–4150 (2017).
23. M. L. Gorodetsky and V. S. Ilchenko, "Optical microsphere resonators: optimal coupling to high-Q whispering-gallery modes," J. Opt. Soc. Am. B **16**, 147–154 (1999).
24. D. Huang, L. Shi, M. Liu, M. Deng, T. Zhu, and W. Huang, "In-fiber whispering-gallery-mode resonator fabricated by femtosecond laser micromachining," Opt. Lett. **40**, 3770–3773 (2015).
25. G. N. Conti, S. Berneschi, F. Cosi, S. Pelli, S. Soria, G. C. Righini, P.-H. Merrer, M. Dispenza, and A. Secchi, "Coupling of angle polished waveguides to high-Q whispering gallery mode resonators," in *The European Conference on Lasers and Electro-Optics* (Optical Society of America, 2011), paper CK_P9.
26. T. Siegle, J. Kellerer, M. Bonenberger, S. Krämmer, C. Klusmann, M. Müller, and H. Kalt, "Comparison of various excitation and detection schemes for dye-doped polymeric whispering gallery mode microlasers," Opt. Express **26**, 3579–3593 (2018).
27. X. Jiang, L. Shao, S. X. Zhang, X. Yi, J. Wiersig, L. Wang, Q. Gong, M. Lončar, L. Yang, and Y. F. Xiao, "Chaos-assisted broadband momentum transformation in optical microresonators," Science **358**, 344–347 (2017).
28. F. Monifi, S. K. Özdemir, J. Friedlein, and L. Yang, "Encapsulation of a fiber taper coupled microtoroid resonator in a polymer matrix," IEEE Photon. Technol. Lett. **25**, 1458–1461 (2013).
29. A. Francois, K. J. Rowland, and T. M. Monro, "Highly efficient excitation and detection of whispering gallery modes in a dye-doped microsphere using a microstructured optical fiber," Appl. Phys. Lett. **99**, 141111 (2011).
30. K. Kosma, G. Zito, K. Schuster, and S. Pissadakis, "Whispering gallery mode microsphere resonator integrated inside a microstructured optical fiber," Opt. Lett. **38**, 1301–1303 (2013).
31. R. Wang, M. Fraser, J. Li, X. Qiao, and A. Wang, "Integrated in-fiber coupler for microsphere whispering-gallery modes resonator excitation," Opt. Lett. **40**, 308–311 (2015).
32. H. Wang, X. Lan, J. Huang, L. Yuan, C. W. Kim, and H. Xiao, "Fiber pigtailed thin wall capillary coupler for excitation of microsphere WGM resonator," Opt. Express **21**, 15834–15839 (2013).

33. X. Zhang, Y. Yang, H. Shao, H. Bai, F. Pang, H. Xiao, and T. Wang, "Fano resonances in cone-shaped inwall capillary based microsphere resonator," Opt. Express **25**, 615–621 (2017).
34. X. Zhang, Y. Yang, H. Bai, J. Wang, M. Yan, H. Xiao, and T. Wang, "Theoretical aspects and sensing demonstrations of cone-shaped inwall capillary-based microsphere resonators," Photon. Res. **5**, 516–520 (2017).
35. A. Zhou, B. Qin, Z. Zhu, Y. Zhang, Z. Liu, J. Yang, and L. Yuan, "Hybrid structured fiber-optic Fabry-Perot interferometer for simultaneous measurement of strain and temperature," Opt. Lett. **39**, 5267–5270 (2014).
36. J. Yang, L. Yuan, S. Cao, and X. Zhu, "Coupling model of standard single-mode and capillary fiber," Appl. Opt. **48**, 5624–5628 (2009).
37. X. Zhang, H. Bai, H. Pan, J. Wang, M. Yan, H. Xiao, and T. Wang, "In-line fiber Michelson interferometer for enhancing the Q factor of cone-shaped inwall capillary coupled resonators," IEEE Photon. J. **10**, 6801808 (2018).
38. F. Shu, X. Jiang, G. Zhao, and L. Yang, "A scatterer-assisted whispering-gallery-mode microprobe," Nanophotonics **7**, 1455–1460 (2018).